Corrosion of Ni in 1-butyl-1-methyl-pyrrolidinium bis (trifluoromethylsulfonyl) amide room-temperature ionic liquid: An in situ X-ray imaging and spectromicroscopy study

ARTICLE *in* PHYSICAL CHEMISTRY CHEMICAL PHYSICS · MARCH 2011

Impact Factor: 4.49 · DOI: 10.1039/c0cp02618b · Source: PubMed

PCCP

Dynamic Article Links

Cite this: *Phys. Chem. Chem. Phys.*, 2011, **13**, 7968–7974

www.rsc.org/pccp

PAPER

Corrosion of Ni in 1-butyl-1-methyl-pyrrolidinium bis (trifluoromethylsulfonyl) amide room-temperature ionic liquid: an *in situ* X-ray imaging and spectromicroscopy study

Benedetto Bozzini,*[a] Alessandra Gianoncelli,[b] Burkhard Kaulich,[b] Maya Kiskinova,[b] Claudio Mele[a] and Mauro Prasciolu[c]

Received 22nd November 2010, Accepted 1st March 2011
DOI: 10.1039/c0cp02618b

This paper reports a pioneering application of soft X-ray scanning transmission microscopy (STXM), combined with micro-spot X-ray absorption spectroscopy (XAS) and X-ray fluorescence spectroscopy (XRF), for the investigation of the corrosion of metal electrodes in contact with room-temperature ionic liquids (RTIL). Using an open electrochemical cell *in vacuo* we explore some fundamental aspects of the aggressiveness of the 1-butyl-1-methyl-pyrrolidinium bis(trifluoromethylsulfonyl)amide ([BMP][TFSA]) RTIL towards Ni under *in situ* electrochemical polarisation. The possibility of imaging electrochemically-induced morphological features in conjunction with micro-XAS and XRF spectroscopies has provided unprecedented details regarding the space distribution and chemical state of corrosion products.

1. Introduction

Room-temperature ionic liquids (RTIL) are experiencing notable research interest as advanced solvents and electrolytes in several fields, among which electrochemistry is a rapidly developing one, with many potential applications in: lithium batteries, solar cells and fuel cells, electrodeposition of metals, alloys and semiconductors as well as electrosynthesis of organics and polymers.[1–3] The study and characterisation of the properties of surface layers formed by RTILs on engineering materials are highly relevant for many industrial applications, such as the choice of materials for chemical plant components and counter electrodes.

The corrosion behaviour of several metals and alloys in various ionic liquids has already been studied by electrochemical,[4–17] spectroscopic (secondary ion mass spectrometry (SIMS) and X-ray photoelectron spectroscopy (XPS)[18,19] and gravimetric[4–7,11,20] methods, as well as by morphological analysis techniques.[4,7,8,11,13,21,22] A detailed list of the systems addressed in the literature is reported in Table 1. The corrosivity of RTIL media strongly depends on the chemical nature of the cationic and anionic moieties;[20] furthermore, the presence of water plays a crucial role.[11] High corrosion resistance with respect to RTILs was reported for a number of metals and alloys: stainless steel is resistant in anhydrous systems as well as in the presence of traces of water[9,20] and localized corrosion was attributed to the presence of Cl^-;[9] copper, nickel, AISI 1018 steel, brass and Inconel 600 show low corrosion current densities in 1-butyl-3-methyl-imidazolium bis-(trifluoromethanesulfonyl)imide ($[C_4mim][Tf_2N]$) at room temperature; magnesium and the AZ91 alloys, both characterised by tremendous corrosion rates in aqueous solutions, are practically inert in anhydrous 1-butyl-3-methylimidazolium trifluoromethylsulfonate;[22] aluminium corrosion was found to be negligible in RTILs electrolytes containing LiTFSI, considered for the replacement of EC/DMC in lithium ion batteries.[8,16,23] The expected, ubiquitous enhancing effect of high temperature has been highlighted.[4,7,20] Surface treatments based on RTILs have also been proposed as methods for the control of the corrosion of magnesium, magnesium alloys,[24–27] carbon,[18,28–31] stainless steel,[26,32] nickel alloys[33] and copper alloys.[18]

In this paper we investigated the electrochemical corrosion of Ni in contact with 1-butyl-1-methyl-pyrrolidinium bis (trifluoromethylsulfonyl) amide ([BMP][TFSA]) *in vacuo*. This RTIL was considered because it is gaining momentum in electrodeposition applications owing to its hydrophobic character, good stability to comparatively high temperatures and hydrolysis as well as the wide electrochemical window. Nevertheless, to our knowledge no information is available about its behavior in the anodic processes that accompany electrodeposition: in particular the anodic efficiency of Ni and other metals is not known, as well as their possible corrosion modes; moreover, no guidelines are available for the choice of materials for insoluble anodes.

This study was carried out by synchrotron-based soft X-ray transmission microscopy (STXM), coupled with micro-spot

[a] *Dipartimento di Ingegneria dell'Innovazione, Università del Salento, via Monteroni, 73100 Lecce, Italy*
[b] *Elettra-Sinctrotrone Trieste SCpA, S.S. 14, km 163.5 in Area Science Park, 34149 Basovizza (TS), Italy*
[c] *CNR-IOM, S.S.14 Km 163.5, Area Science Park, 34149 Basovizza (TS), Italy*

Table 1 List of published studies of metal corrosion in ionic liquids

Reference	Metal	Ionic liquid
4	Copper, nickel, AISI 1018, brass, Inconel 600	1-Butyl-3-methyimidazolium bis(trifluoromethylsulfonyl) amide
5	Copper	1-Butyl-3-methyl imidazolium bromide monohydrate
6	Silver	1-Butyl-3-methyl-imidazolium bromide monohydrate
7	AISI 316	1-Hexyl-3-methylimidazolium tris(pentafluoroethyl)trifluorophosphate
	AISI 1018	1-Butyl-1-methylpyrrolidinium trifluoromethylsulfonate
		Ethyl-dimethyl-propylammonium bis(trifluoromethylsulfonyl) amide
		1-Butyl-1-methylpyrrolidinium bis (trifluoromethylsulfonyl) amide
8,16	Aluminium	1-Alkyl-3-methylimidazolium bis[(trifluoromethyl)sulfonyl] amide
9	AISI 316	1-Octyl-3-methylimidazolium hexafluorophosphate
	AISI 1018	1-Butyl-3-methylimidazolium bis(trifluoromethylsulfonyl) amide
		1-Butyl-3-methylimidazolium chloride
10	Magnesium	Choline chloride/urea
		Choline chloride/ethylene glycol
		Choline chloride/glycerol
		Choline chloride/malonic acid
		Choline chloride/zinc chloride
11	Aluminium alloy Al2011	Alkylimidazolium ILs
12	Niobium, tantalum	1-Butyl-3-methyimidazolium bromide
13	Lead–antimony–tin alloy	Triethyl ammonium hydrogen sulfate
		Dibutyl ammonium hydrogen sulfate
		Benzylammonium hydrogen sulfate
		1-Butyl-3-methylimidazolium hydrogen sulfate
14,15	Anodic porous alumina	1-Butyl-3-methylimidazolium 2-(2-methoxyethoxy) ethyl sulfate
		1-Butyl-3-methylimidazolium tetrafluoroborate
17	Titanium	1-Ethyl-3-methylimidazolium chloride
18	Inconel 600, Naval brass, AISI 1018	1-Butyl-3-methylimidazolium bis(trifluoromethylsulfonyl) amide
20	Carbon steel, austenitic stainless steel, Hastelloy C22, copper, brass, aluminium	1-Butyl-3-methylimidazolium chloride
		ECOENG 212
		EMIMTOS
		ECOENG 418
		AMMOENG 100
		TEGOTAIN 3300
21	Copper	1-Octyl-3-methylimidazolium hexafluorophosphate
22	Magnesium, AZ91D magnesium alloy	1-Butyl-3-methylimidazolium trifluoromethylsulfonate
23	Aluminium	1-Ethyl-3-methylimidazolium bis(trifluoromethylsulfonyl) amide + lithium bis(trifluoromethylsulfonyl) amide
25	Magnesium	(Tetradecyl)phosphonium diphenylphosphate

X-ray absorption spectroscopy (XAS) and X-ray fluorescence spectroscopy (XRF) allowing *in situ* characterisation of complex multi-material systems in electrochemical environments by sub-micrometre lateral resolution.[34–38] Thanks to the properties of this RTIL, an open electrochemical cell can be used *in vacuo* to perform *in situ* XRF measurements.

The possibility of carrying out measurements on RTILs *in vacuo* has already been recognised by previous XPS,[39–41] soft X-ray emission spectroscopy,[42] and underpotential deposition work.[43] As far as *in situ* microscopy work with RTILs is concerned, it is worth recalling that Ag electrodeposition from BMI-TFSI was followed by *in situ* SEM.[44] To our knowledge, the present paper is the first report demonstrating the potential of soft X-ray imaging and spectromicroscopy, based on monitoring the transmitted and emitted X-rays, to explore the corrosion of the working Ni electrodes and mass transport and lateral distribution of the corrosion products in the RTIL media.

2. Experimental

The cell geometry and the arrangement of the thin film electrodes are depicted in Fig. 1. As noted above, we employed an open electrochemical cell, based on the design proposed and described in detail elsewhere.[35,36] The cell consists of a Si_3N_4 optical window onto which two square, 40 nm thick Au and 75 nm thick Ni electrodes are evaporated. The Ni electrodes acted as working electrodes and the Au electrodes were employed as a counter-electrode and quasi-reference-electrode (QRE), respectively. All the potentials are reported on the Au QRE scale. Lateral electrolyte containment was insured by a

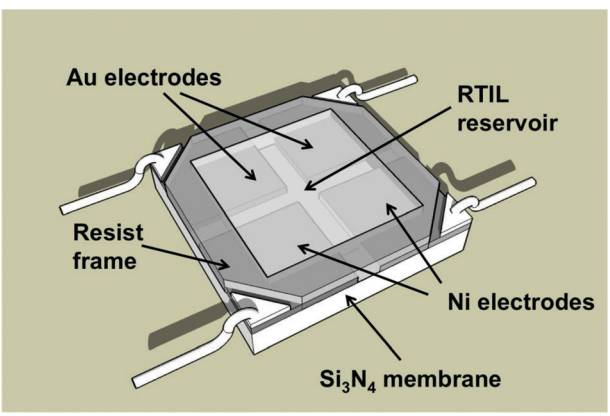

Fig. 1 Schematic view of the electrochemical cell, highlighting electrode and electrolyte layout. Figure details not to scale.

500 nm thick resist layer, deposited on top of the X-ray window/electrode assembly, before application of the electrolyte film. This cell configuration allows working with an X-ray beam crossing the electrode/electrolyte assembly normally to the optical window, the transmitted X-rays can thus be monitored by the detector placed behind the cell. The RTIL was spun on the lithographed electrode assembly, in order to achieve a thickness of 200 nm, optimal for detection of transmitted X-rays and emitted fluorescence signal from the electrodes immersed in the electrolyte. The 3D primary current–density distribution has been computed by the COMSOL multiphysics solver, based on the finite-element method.[36]

The molecular geometry of [BMP][TFSA] (shown in Fig. 2) has been estimated by quantum chemical computations in the framework of the Density Functional Theory (DFT), as implemented in the Gaussian 03 package,[45] with the B3LYP hybrid functional, and basis set 6-311++.

The occurrence of morphological and chemical changes, related to the relevant corrosion processes, have been verified by imaging and spectromicroscopy analyses carried out with the Scanning module of the TwinMic X-ray microscope at the Elettra synchrotron facility, Trieste, Italy, operated in the 400–2200 keV energy range in a vacuum of 10^{-6} mbar.[46,47] In STXM, the X-ray beam can be focused down to sub-100 nm spot size by zone plate diffractive optics and the specimen is raster-scanned across the X-ray probe for obtaining 2D images. The microscope is equipped with a Low Energy XRF spectroscopy system, providing elemental maps[48,49] correlated to the simultaneously acquired morphology (absorption and phase contrast) images. The XRF maps are complementary to the X-ray absorption spectroscopy analysis of areas selected from the maps. In the present study the X-ray probe size was varied between 200 nm and 1 μm, according to the dimensions of the features of interest. The X-ray absorption and phase contrast images were recorded by a IXON Andor-Technology EMCCD camera providing simultaneously absorption and phase information.[50]

It is worth noting that highly focussed soft X-rays from synchrotron sources may give rise to beam-induced damaging of organic matter:[51] in particular, bond-breaking in RTILs has been pinpointed.[39,52] However, in our study we do not mean to focus on the details of the RTIL chemistry, but rather on the corrosion of the electrodes and the possible mass transport of the corrosion products in the RTIL medium: in this respect we reckon that beam-damage effects on the RTIL have a minor impact, since the quantities we are probing are the chemical state and lateral distribution of Ni species, that are stable under irradiation. Moreover, it is important to stress that irradiation damaging possibly giving rise to charging effects can be disturbing in XPS, a photon-in/electron-out surface-sensitive technique;[39] this can also have a bearing on mass-transport results investigated by XPS.[19] Nevertheless, since the spectroscopy we are employing in our present study is a photon-in/photon-out method responsive to the sample bulk, RTIL beam-damage can be regarded as a higher order effect.

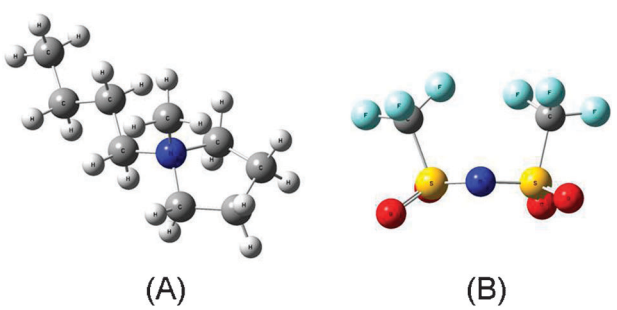

Fig. 2 Molecular structure of 1-butyl-1-methyl-pyrrolidinium bis-(trifluoromethylesulfonyl) amide ([BMP][TFSA]): (A) BMP^+ (equatorial conformation), (B) $TFSA^-$ (*cis* conformation), as computed by DFT.

3. Results and discussion

3.1 Optical microscopy

After applying electrochemical polarisation, the corrosion of Ni electrodes was followed *in situ* by (i) optical microscopy in a cell, sealed as in ref. 2, mounted in an Ar-filled dry-box and (ii) recording of the corrosion current. Characterisation by optical microscopy, exhibiting a faster acquisition rate in the meso-scopic range than STXM, is adequate for the assessment of the dynamics of morphological changes. Fig. 3 shows a sequence of *in situ* optical micrographs, recorded during the initial stages of the corrosion process for a Ni electrode. We found that the Ni electrode does not show any observable damage for potentials lower than 500 mV. At 500 mV, pits start to form: this damage localisation is attributed to the current density distribution prevailing in the relevant thin-layer cell geometry.[36] The stripping charge, derived from an integrated potentiostatic current transient, is shown in Fig. 4. Under the hypothesis of 100% anodic current efficiency, the total

Fig. 3 Optical micrographs of a Ni electrode during corrosion at an anodic polarisation of 500 mV *vs.* Au QRE.

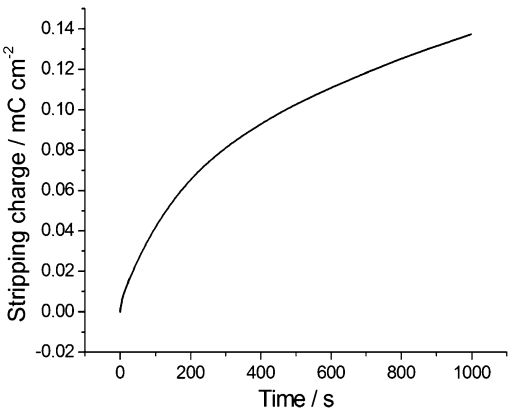

Fig. 4 Stripping charge as a function of time during the potentiostatic corrosion of a Ni thin film electrode at 500 mV *vs.* Au QRE.

integrated charge during 1000 s of measurement corresponds to 59 nm; it can thus be concluded that Ni polarised at 500 mV is completely oxidised. We focussed on this condition for our *in situ* TXM measurements.

3.2 X-Ray imaging, micro-XRF and micro-XAS

In Fig. 5a we report three absorption images (A–C)—recorded at the Ni L-edge (C) and above it (A and B) (the dark area corresponds to the Ni electrode)—and the corresponding absorption intensity variations across the electrode edges, illustrated by the profile plots. Using photon energy above the Ni L-edge allows detection of the emitted Ni L fluorescence signal, which also provides simultaneous chemical information. The contrast of these absorption images provides information on spatial thickness variations of the Ni electrode as well as on the spreading of stronger-absorbing Ni-containing species in the electrolyte, released from the electrode by corrosion. Image A and the left side of image C show the edge of the Ni electrode facing the Ni auxiliary electrode (low current density region), while image (B) and the bottom of image C show the edge facing the Au counter-electrode (high current density region). The morphological details of the electrolyte and of the electrode can be better appreciated in the corresponding phase contrast images, shown in Fig. 5b.

Differences in corroded electrode morphology (in terms of diffuse interface between the metal electrode and the ionic liquid zone) are clearly highlighted by X-ray absorption profiles (Fig. 5a), taken across the electrode edges and in particular by comparing the vertical and horizontal absorption profiles of the electrode corner image. The absorption images and line profiles suggest generalised thinning, accompanied by the formation of some regions of thicker metal, coherently with the localised-corrosion morphologies imaged, though at a different magnification, by optical microscopy (Fig. 3). Comparing the edge profile slopes found in the low (image A and horizontal scan in image C) and high (image B and vertical scan in image C) current density zones, one can clearly see that the latter are smeared out, indicating thinning due to loss of material. Eventually, stronger X-ray absorbing (darker) spots are also formed in the ionic liquid, close to the corroded electrode, denoting precipitation of corrosion products within the electrolyte.

These observations are complemented by the Ni XRF line scans, shown below the phase contrast images in Fig. 5b.

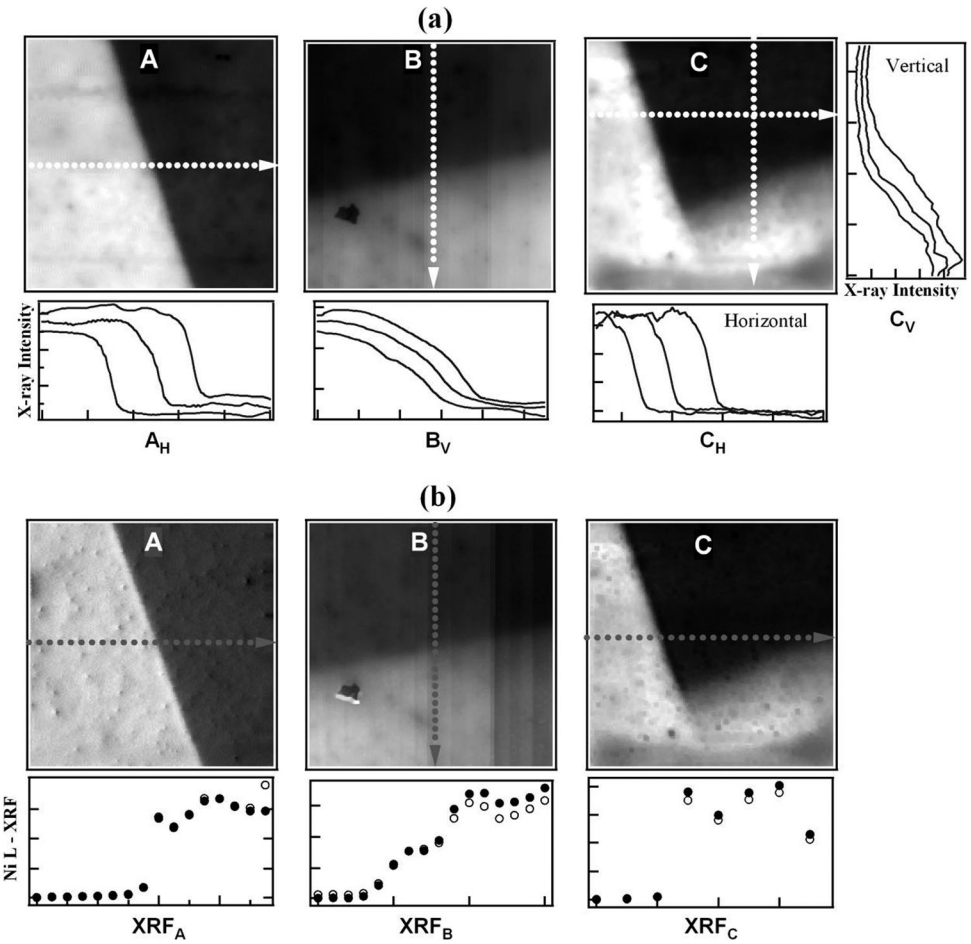

Fig. 5 A choice of typical STXM images (absorption images in (a) with the corresponding horizontal (H) and vertical (V) profile plots (A_H, B_V, C_H and C_V) and phase contrast in (b)), derived from different locations of the Ni electrode and neighbouring electrolyte area. STXM imaging parameters are: $80 \times 80\ \mu m^2$, 160×160 pixels, 10 ms dwell time, beam energy: 852 eV (image of the corner, panel C) and 977 eV (panels A and B). The graphs shown in the bottom of the image (XRF_A, XRF_B and XRF_C) are the Ni XRF intensity along the lines indicated in the phase contrast images (b).

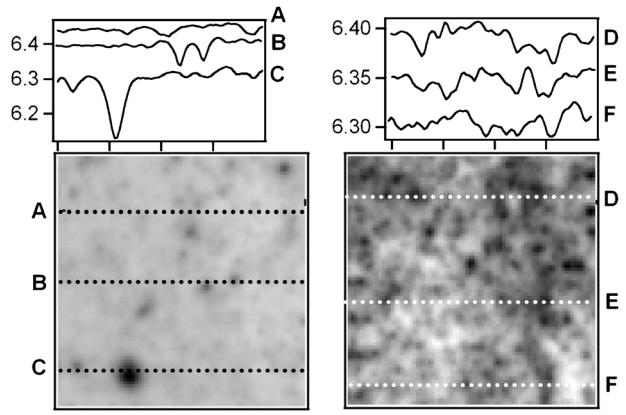

Fig. 6 STXM absorption images with the corresponding profile plots (A, B, C, D, E and F) recorded at typical positions in the central part of the Ni electrode (80 × 80 μm^2, 80 × 80 pixels, 10 ms dwell time, beam energy: 977 eV).

Comparison of the Ni XRF scan plots confirms the more notable Ni depletion from the electrode edge facing the Au counter-electrode. In brief, both the absorption intensity profiles and XRF line scans reveal the residual morphology of the electrode edge; comparing the Ni concentration gradients one can prove injection of metal into the electrolyte, related to the corrosion process, and detect some dips in the Ni content inside the electrode, evidenced by the absorption maps, indicative of localised corrosion processes.

The contrast variations in the absorption images taken in the central part of the electrode (Fig. 6) also show localised corrosion, with different degrees of thinning, clearly manifested by the line profiles. In both images one can notice Ni density variations that can be related to the pitting behaviour observed by optical microscopy (Fig. 3).

3.3 XAS spectromicroscopy

The X-ray transmission imaging and XRF results have been complemented with XAS spectromicroscopy that provides additional information about the changes in the oxidation state of Ni injected in the electrolyte. Fig. 7 shows a set of Ni L_3 XAS spectra, measured in several points, indicated in the STXM image. These spectra represent the Ni chemical state and local concentration inside the Ni electrode (A, B) and in the near-edge region of the bottom electrode corner (C, D) which—as discussed above—is more severely corroded. The intensity of the XAS spectra confirms the concentration gradient manifested by the XRF data; *i.e.* comparing the spectral integral areas, the amount of Ni injected in the electrolyte region in the vicinity of the electrode is about 4.5 times less than the Ni content of the inner part of the electrode. Another notable feature that is highlighted by the comparison of the spectra is their different lineshape, indicating that Ni injected into the electrolyte also changes its chemical state. The Ni L_3 spectra taken in locations corresponding to the initial position of the as-fabricated electrode (points A and B) appear similar to the previously reported ones for non-corroded electrodes that were passivated with a relatively thick NiO layer.[37] In fact, the deconvolution of the Ni L_3 spectra taken in points A and B can be carried out considering the reported spectra corresponding to Ni^0 (single component at ~853.1 eV) and Ni(II) (two components at ~854 eV and 855.8 eV).[37,53] The Ni L_3 spectra corresponding to the diffuse shade projecting out of the electrode (points C and D) towards the Au counter-electrode have apparently different shapes and their deconvolution requires components that are indicative of the presence of Ni^{3+} chemical state, in particular, the 'pre-edge' feature is especially diagnostic.[54] Coherently with the expected current density distribution,[36] only traces of Ni (about 8 times less than in points C and D) are present in the electrolyte zone close to the corner (point E) of the electrode not facing the counter electrode, and no Ni was found away from the corner (point F). The lineshape of the Ni L_3 spectrum, measured in E, is also indicative for traces of Ni^{3+}.

In brief, the XAS and XRF results point to the fact that Ni corrosion products tend to interact with the RTIL, resulting in localisation within the electrolyte zone close to the electrode and changing the Ni valence state. The localisation of the higher-valency form of oxidised Ni in the high-current density region is coherent with the fact that higher anodic potentials develop there. The formation of Ni^{3+}-containing species is known in the electrochemistry of Ni in aqueous solution, mainly relating to secondary passivation by formation of Ni_2O_3 at potentials in excess of 1.5 V_{SCE}: both liquid-phase and solid forms are known.[55] The complex-formation chemistry of Ni(III) in RTILs has not been reported in the literature, to the best of the authors' knowledge, but its

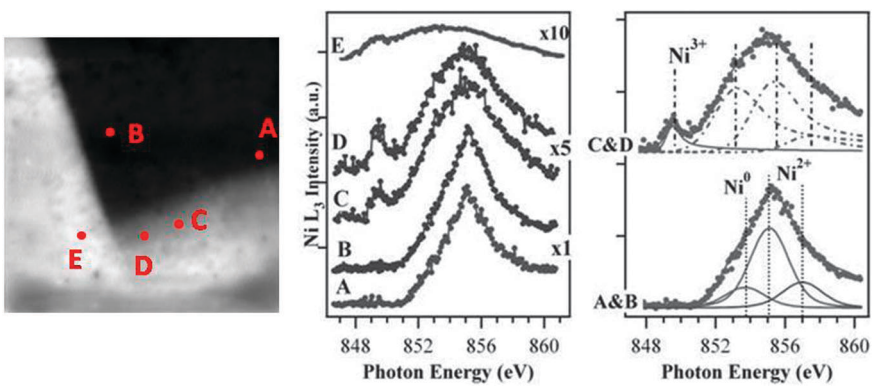

Fig. 7 Localised XAS spectra (measurement time: 1 minute/spectrum) measured in the neighbourhood of the corroded Ni electrode, at the indicated locations (A and B on the Ni electrode, C, D and E in the proximity of the electrode).

stabilisation by binding to organics in non-aqueous systems can be expected on the basis of information available from organometallic chemistry.[56] It should also be considered that in the micro-spot spectroscopy mode the X-ray radiation can induce bond-breaking in the RTIL, forming more or less reactive organic radicals.[39,52] Of course, this can affect the details of chemical state of the metal corrosion products, but their effect on mass transport and lateral distribution can be safely regarded as a higher-order effect.

4. Conclusions

In this paper we report a synchrotron-based *in situ* soft X-ray imaging and spectromicroscopy investigation of the electrochemical corrosion of Ni in [BMP][TFSA] RTIL. The results yield fundamental information, relevant to the design of RTIL-handling facilities and on the technology of soluble and insoluble anodes for electroplating from RTIL-based baths. Ni films of nanometric thickness were corroded in the potentiostatic mode in the thin-layer configuration suitable for *in situ* measurements. The enthalpy of vaporisation of [BMP][TFSA] allowed working with an open cell *in vacuo,*[57] and performing *in situ* XRF measurements during the electrochemical process. Morphological and chemical details of the corrosion process and of the precipitation of corrosion products in the RTIL layer adjoining the electrode are obtained from X-ray absorption images as well as XAS and XRF spectromicroscopy. This multi-technique approach pinpoints the release of corrosion products to the electrolyte phase as well as the formation of Ni^{2+} and Ni^{3+} in regions exhibiting lower and higher current densities, respectively, and correspondingly different degrees of anodic polarisation. This is the first *in situ* investigation of the electrochemical behaviour of a RTIL using X-ray microscopy methods, not only proving the power of this approach for the understanding of the investigated system, but also its potential to exploit the electrochemical processes carried out with RTIL-based electrolytes.

References

1 *Electrochemical Aspects of Ionic Liquids*, ed. H. Ohno, Wiley Interscience, Hoboken, NJ, 2005.
2 *Electrodeposition from Ionic Liquids*, ed. F. Endres, D. MacFarlane and A. Abbott, Wiley-VCH, Weinheim, 2008.
3 *Trans. Inst. Met. Finish.*, special issue: Plating from ionic liquids, July 2008, 86(4).
4 I. Perissi, U. Bardi, S. Caporali and A. Lavacchi, *Corros. Sci.*, 2006, **48**, 2349.
5 E. P. Grishina, L. M. Ramenskaya, T. V. Vladimirova and A. M. Pimenova, *Russ. J. Appl. Chem.*, 2007, **80**, 248.
6 E. P. Grishina, T. V. Vladimirova, L. M. Ramenskaya and K. S. Shilovskii, *Russ. J. Electrochem.*, 2007, **43**, 234.
7 I. Perissi, U. Bardi, S. Caporali, A. Fossati and A. Lavacchi, *Sol. Energy Mater. Sol. Cells*, 2008, **92**, 510.
8 C. Peng, L. Yang, Z. Zhang, K. Tachibana, Y. Yang and S. Zhao, *Electrochim. Acta*, 2008, **53**, 4764.
9 R. G. Reddy, Z. J. Zhang, M. F. Arenas and D. M. Blake, *High Temp. Mater. Processes*, 2003, **22**, 87.
10 A. Bakkar and V. Neubert, *Electrochem. Commun.*, 2007, **9**, 2428.
11 M.-D. Bermúdez, A.-E. Jiménez and G. Martínez-Nicolás, *Appl. Surf. Sci.*, 2007, **253**, 7295.
12 E. P. Grishina, L. M. Ramenskaya and A. M. Pimenova, *Russ. J. Electrochem.*, 2008, **44**, 213.
13 B. Rezaei, S. Mallakpour and M. Taki, *J. Power Sources*, 2009, **187**, 605.
14 M. Salerno, N. Patra and R. Cingolani, *Nanoscale Res. Lett.*, 2009, **4**, 865.
15 M. Salerno, N. Patra, R. Losso and R. Cingolani, *Mater. Lett.*, 2009, **63**, 1826.
16 C. Peng, L. Yang, Z. Zhang, K. Tachibana and Y. Yang, *J. Power Sources*, 2007, **173**, 510.
17 M. Ueda, T. Ohtsuka, K. Kuroda, R. Ichino and M. Okido, *Trans. Mater. Res. Soc. Jpn.*, 2008, **33**, 779.
18 A. B. Tolstoguzov, U. Bardi and S. P. Chenakin, *Bull. Russ. Acad. Sci. Phys.*, 2008, **72**, 605.
19 F. Qiu, A. W. Taylor, S. Men, I. J. Villar-Garcia and P. Licence, *Phys. Chem. Chem. Phys.*, 2010, **12**, 1982.
20 M. Uerdingen, C. Treber, M. Balser, G. Schmitt and C. Werner, *Green Chem.*, 2005, **7**, 321.
21 N. Liu, D. Wu, H. Wu, F. Luo and J. Chen, *Solid State Sci.*, 2008, **10**, 1049.
22 A. Shkurankov, S. Z. El Abedin and F. Endres, *Aust. J. Chem.*, 2008, **60**, 35.
23 B. Garcia and M. Armand, *J. Power Sources*, 2004, **132**, 206.
24 N. Birbilis, P. C. Howlett, D. R. MacFarlane and M. Forsyth, *Surf. Coat. Technol.*, 2007, **201**, 4496.
25 P. C. Howlett, W. Neil, T. Khoo, J. Sun, M. Forsyth and D. R. MacFarlane, *Isr. J. Chem.*, 2008, **48**, 313.
26 U. Bardi, S. P. Chenakim, A. Lavacchi, C. Pagura and A. Tolstogouzov, *Appl. Surf. Sci.*, 2006, **252**, 7373.
27 J. L. Goldman and A. B. McEwen, *Electrochem. Solid-State Lett.*, 1999, **2**, 501.
28 S. Caporali, A. Fossati, A. Lavacchi, I. Perissi, A. Tolstoguzov and U. Bardi, *Corros. Sci.*, 2008, **50**, 534.
29 Q. B. Zhang and Y. X. Hua, *Electrochim. Acta*, 2009, **54**, 1881.
30 A. E. Jiménez, M. D. Bermúdez, P. Iglesias, F. J. Carrión and G. Martínez-Nicolás, *Wear*, 2006, **260**, 766.
31 A. E. Jiménez, M. D. Bermúdez, F. J. Carrión and G. Martínez-Nicolás, *Wear*, 2006, **261**, 347.
32 J. Qu, J. J. Truhan, S. Dai, H. Luo and P. J. Blau, *Tribol. Lett.*, 2006, **22**, 207.
33 S. Zein El Abedin, U. Welz-Biermann and F. Endres, *Electrochem. Commun.*, 2005, **7**, 941.
34 D. Guay, J. Stewart-Ornstein, X. Zhang and A. P. Hitchcock, *Anal. Chem.*, 2005, **77**, 3479.
35 B. Bozzini, L. D'Urzo, A. Gianoncelli, B. Kaulich, M. Kiskinova, M. Prasciolu and A. Tadjeddine, *Electrochem. Commun.*, 2008, **10**, 1680.
36 B. Bozzini, L. D'Urzo, A. Gianoncelli, B. Kaulich, M. Prasciolu, I. Sgura, E. Tondo and M. Kiskinova, *J. Phys. Chem. C*, 2009, **113**, 9783.
37 B. Bozzini, A. Gianoncelli, B. Kaulich, M. Kiskinova, M. Prasciolu and I. Sgura, *ChemSusChem*, 2010, **3**, 846.
38 A. Gianoncelli, B. Kaulich, M. Kiskinova, M. Prasciolu, L. D. Urzo and B. Bozzini, *Micron*, 2011, **42**, 342.
39 K. R. J. Lovelock, I. J. Villar-Garcia, F. Maier, H.-P. Steinrück and P. Licence, *Chem. Rev.*, 2010, **110**, 5158.
40 T. Torimoto, T. Tsuda, K. Okazaki and S. Kuwabata, *Adv. Mater.*, 2010, **22**, 1196.
41 S. Kuwabata, T. Tsuda and T. Torimoto, *J. Phys. Chem. Lett.*, 2010, **21**, 3177.
42 K. Kanai, T. Nishi, T. Iwahashi, Y. Ouchi, K. Seki, Y. Harada and S. Shin, *J. Chem. Phys.*, 2008, **129**, 224507.
43 M. Johnston, J.-J. Lee, G. S. Chottiner, B. Miller, T. Tsuda, C. L. Hussey and D. A. Scherson, *J. Phys. Chem. B*, 2005, **109**, 11296.
44 S. Arimoto, H. Kageyama, T. Torimoto and S. Kuwabata, *Electrochem. Commun.*, 2008, **10**, 1901.
45 M. J. Frisch, G. W. Trucks, H. B. Schlegel, G. E. Scuseria, M. A. Robb, J. R. Cheeseman, J. A. Jr. Montgomery, T. Vreven, K. N. Kudin, J. C. Burant, J. M. Millam, S. S. Iyengar, J. Tomasi, V. Barone, B. Mennucci, M. Cossi, G. Scalmani, N. Rega, G. A. Petersson, H. Nakatsuji, M. Hada, M. Ehara, K. Toyota, R. Fukuda, J. Hasegawa, M. Ishida, T. Nakajima, Y. Honda, O. Kitao, H. Nakai, M. Klene, X. Li, J. E. Knox, H. P. Hratchian, J. B. Cross, V. Bakken, C. Adamo, J. Jaramillo, R. Gomperts, R. E. Stratmann, O. Yazyev, A. J. Austin, R. Cammi, C. Pomelli, J. W. Ochterski,

P. Y. Ayala, K. Morokuma, G. A. Voth, P. Salvador, J. J. Dannenberg, V. G. Zakrzewski, S. Dapprich, A. D. Daniels, M. C. Strain, O. Farkas, D. K. Malick, A. D. Rabuck, K. Raghavachari, J. B. Foresman, J. V. Ortiz, Q. Cui, A. G. Baboul, S. Clifford, J. Cioslowski, B. B. Stefanov, G. Liu, A. Liashenko, P. Piskorz, I. Komaromi, R. L. Martin, D. J. Fox, T. Keith, M. A. Al-Laham, C. Y. Peng, A. Nanayakkara, M. Challacombe, P. M. W. Gill, B. Johnson, W. Chen, M. W. Wong, C. Gonzalez and J. A. Pople, *Gaussian03*, Gaussian, Inc., Pittsburgh, PA, 2003.

46 B. Kaulich, D. Bacescu, J. Susini, C. David, E. Di Fabrizio, G. R. Morrison, P. Charalambous, J. Thieme, T. Wilhein, J. Kovac, D. Cocco, M. Salome, O. Dhez, T. Weitkamp, S. Cabrini, D. Cojoc, A. Gianoncelli, U. Vogt, M. Podnar, M. Zangrando, M. Zacchigna and M. Kiskinova, *Proceedings of the 8th Int. Conf. X-ray Microscopy IPAP Conf. Series*, 2006, **7**, 22.

47 www.elettra.trieste.it/twinmic.

48 R. Alberti, T. Klatka, A. Longoni, D. Bacescu, A. Marcello, A. De Marco, A. Gianoncelli and B. Kaulich, *X-Ray Spectrom.*, 2009, **38**, 205.

49 A. Gianoncelli, B. Kaulich, R. Alberti, T. Klatka, A. Longoni, A. de Marco, A. Marcello and M. Kiskinova, *Nucl. Instrum. Methods Phys. Res., Sect. A*, 2009, **608**, 195.

50 G. R. Morrison, A. Gianoncelli, B. Kaulich, D. Bacescu and J. Kovac, in *A fast-readout CCD system for configured-detector imaging in STXM*, in Proc. 8th Int. Conf. X-ray microscopy, ed. S. Aoki, Y. Kagoshima and Y. Suzuki, Conf. Proc. Series IPAP 7, pp. 377–379.

51 L. Gregoratti, T. O. Mentes, A. Locatelli and M. Kiskinova, *J. Electron Spectrosc. Relat. Phenom.*, 2009, **170**, 13.

52 A. Keppler, M. Himmerlich, T. Ikari, M. Marschewski, E. Pachomow, O. Höfft, W. Maus-Friedrichs, F. Endres and S. Krischok, *Phys. Chem. Chem. Phys.*, 2011, **13**, 1174.

53 C. Sorg, N. Ponpandian, A. Scherz, H. Wende, R. Nünthel, T. Gleitsmann and K. Baberschke, *Surf. Sci.*, 2004, **565**, 197.

54 I. Preda, M. Abbate, A. Gutierrez, S. Palacın, A. Vollmer and L. Soriano, *J. Electron Spectrosc. Relat. Phenom.*, 2007, **156–158**, 111.

55 M. E. G. Lyons and M. P. Brandon, *Int. J. Electrochem. Sci.*, 2008, **3**, 1386.

56 Ch.-M. Lee, Ch.-H. Chen, F.-X. Liao, Ch.-H. Hu and G.-Hs. Lee, *J. Am. Chem. Soc.*, 2010, **132**, 9256.

57 A. Deyko, K. R. J. Lovelock, J.-A. Corfield, A. W. Taylor, P. N. Gooden, I. J. Villar-Garcia, P. Licence, R. G. Jones, V. G. Krasovskiy, E. A. Chernikova and L. M. Kustov, *Phys. Chem. Chem. Phys.*, 2009, **11**, 8544.

